ACCSCIENCE PUBLISHING

Materials Science in Additive Manufacturing

ORIGINAL RESEARCH ARTICLE

Effect of hot isostatic pressing on the microstructure and mechanical properties of porous Ti-6Al-4V alloy manufactured by laser powder bed fusion

Marketa Strakova[1]*, Jiri Kubasek[1], Jonas Divin[1], Jan Pinc[2], and Dalibor Vojtech[1]

[1]Department of Metals and Corrosion Engineering, University of Chemistry and Technology, Prague, Czech Republic

[2]FZU - Institute of Physics of the Czech Academy of Sciences, Prague, Czech Republic

Abstract

Laser powder bed fusion (LPBF) enables the production of Ti-6Al-4V alloys with tailored porous structures, which are beneficial for biomedical applications due to their reduced elastic modulus and enhanced bone integration potential. This study examines the effect of hot isostatic pressing (HIP) on the microstructure and mechanical properties of diamond and gyroid porous structures fabricated by LPBF. Solid tensile specimens served as reference materials. HIP significantly reduced porosity, decreased ultimate tensile strength and hardness, but markedly increased ductility (from 6% to 17%). Compressive strengths reached approximately 100 MPa (diamond) and 240 MPa (gyroid), with HIP causing only a slight increase in strain. However, HIP notably improved bending performance, raising the flexural strength of gyroid structures from 280 MPa (as-printed) to 340 MPa (post-HIP). The strength of LPBF-fabricated Ti-6Al-4V porous structures is reduced by HIP, but their ductility and bending performance are enhanced, making them more suitable for biomedical applications.

Keywords: Ti-6Al-4V; Laser powder bed fusion; Hot isostatic pressing; Porous material; Mechanical properties; Lattice structures

***Corresponding author:**
Marketa Strakova
(strakovm@vscht.cz)

Citation: Strakova M, Kubasek J, Divin J, Pinc J, Vojtech D. Effect of hot isostatic pressing on microstructure and mechanical properties of porous Ti-6Al-4V alloy manufactured by laser powder bed fusion. *Mater Sci Add Manuf*. 2026;5(1):025260055. doi: 10.36922/MSAM025260055

Received: June 27, 2025

Revised: July 25, 2025

Accepted: August 11, 2025

Published online: October 13, 2025

1. Introduction

The aerospace, sporting goods, and petrochemical industries widely use titanium and its alloys, especially Ti-6Al-4V, due to their relatively low density, high strength, and good corrosion resistance.[1-4] Furthermore, this alloy is of particular importance in biomedical engineering because of its great mechanical performance. It also has a high strength-to-weight ratio, low modulus, high fatigue strength, and biocompatibility.[5] Ti-6Al-4V is particularly useful in the manufacture of artificial joints, bone implants, prosthetics, and surgical instruments, offering a good balance of strength, flexibility, and toughness. Aluminum makes the alloy stronger and lighter, while vanadium adds flexibility and stability. The applicability of Ti-6Al-4V alloy in biomedicine, as well as its potential modification to improve surface properties, has been a major topic in scientific research.[1,2,6]

The production process of titanium is so challenging that it makes it more valuable than steel or aluminum. Given the high material costs, it is advantageous to make parts that need very little post-processing.[3] Ti-6Al-4V is also an ideal candidate for innovative production methods, such as powder-based additive manufacturing (AM). In AM, components are fabricated in a net-shape process by fusing successive layers of metallic raw material to a base material using a pre-programmed scanning pattern of a focused laser or electron beam.[5,7,8] The powder can be applied either through powder bed fusion (PBF), which involves spreading and selectively melting individual layers of powder, or through direct energy deposition, which delivers powder continuously to the melt pool through coaxial jets.[9,10] In theory, AM can produce completely dense, three-dimensional components with highly intricate geometries.[11,12] However, AM-fabricated alloy often exhibits relatively high porosity.[12] The rapid melting and solidification inherent to AM vary with part geometry and path planning, and the layered nature of the process introduces non-fusion defects at layer and laser pass interfaces. Consequently, it becomes challenging to manufacture fully dense, defect-free components with consistent mechanical properties across multiple batches. A number of researchers have used hot isostatic pressing (HIP) to reduce pore size and homogenize microstructural properties through post-processing heat treatment.[12,13] Vilaro *et al.*[14] reported that the mechanical behavior of AM Ti-6Al-4V is strongly influenced by its high porosity, with macroscopic ductility strongly affected by pore orientation and shape.

Advances in AM technologies have been rapid, with laser PBF (LPBF) emerging as one of the key PBF techniques for producing the demanding $\alpha + \beta$ Ti-6Al-4V alloy.[15,16] Recent studies highlight LPBF's potential for fabricating multi-material parts with graded layers, significantly affecting interfacial bonding and mechanical integrity.[17] LPBF builds three-dimensional metal parts by melting metallic powders layer by layer with a laser, and the high cooling rate promotes rapid solidification and phase transformations. This method produces parts in the desired shape and size directly, minimizing the need for additional machining.[5,18,19] Its capability to produce complex 3D medical parts with high precision has driven demand for LPBF in biomedical applications.[6] LPBF can also create porous implant models, which can reduce the Young's modulus, mitigate stress shielding, and improve osseointegration.[20] The mechanical response of LPBF-fabricated porous structures can be tuned by varying unit cell geometry and orientation, significantly influencing impact resistance and energy absorption.[21] The porous part helps to avoid stress shielding and provides biological fixation by allowing tissue ingrowth. In addition, porous structures can act as efficient drug delivery reservoirs to suppress post-surgical inflammatory reactions. Thus, incorporating porous parts into implants can help mimic the behavior of human bone.[22] Significant research efforts have been devoted to optimizing both the manufacturing process and surface modification of porous titanium alloys to enhance their performance in medical applications.[23] In a study by Gao *et al.*,[24] porous titanium implants with a gradient modulus were found to increase femoral surface deformation by 17.1%, reducing the stress shield effect, bone loss, and aseptic loosening. Verma *et al.*[25] confirmed that the porous architecture reduced the effective modulus of elasticity by more than 95%, thereby reducing the stress-shielding effect.

Monotonic tensile properties superior to those of conventionally fabricated alloys have been reported for Ti-6Al-4V manufactured by LPBF. However, its fatigue resistance decreases during cyclic loading due to internal porosity.[15,16] Even with optimized parameters, it is not possible to achieve fully dense parts.[6,26] Recent studies have shown that this issue can be addressed by optimizing the microstructure through precise thermal annealing, which can be especially effective in balancing strength and ductility when performed near the β-transus temperature, typically between 700°C (stress-relieved state) and 1080°C (solution-treated state).[14,27-29] In stress-relieved samples, only minimal changes in grain size are observed; however, complete dissolution of martensitic phases occurs during solution treatment, leading to the formation of an equilibrium ($\alpha + \beta$) microstructure.[19] A comprehensive review of additively manufactured titanium alloys confirms that their microstructure, defect distribution, and mechanical properties are highly dependent on the AM technique employed and the subsequent post-processing conditions.[30] Thermal annealing also produces the expected grain refinement.[19] With increasing annealing temperature, tensile strength initially increases and then decreases, with a similar trend observed in elongation data.[16]

Thermomechanical HIP has also been demonstrated to be effective in minimizing defects associated with porosity in LPBF-printed components.[31] HIP is a process that applies high pressure and temperature evenly to materials in a high-pressure container, which helps to remove internal porosity, improve material density, and enhance mechanical properties.[32-34] Increasing HIP pressure promotes the formation of the β phase, while higher HIP temperatures lead to a reduction in the amount of α and β phases. Simultaneously, the tensile strength and yield strength of LPBF-produced Ti-6Al-4V

decrease as the HIP temperature rises.[35] HIP treatment is also known to eliminate microstructural differences across layers in Ti-6Al-4V, resulting in α + β layered structures that enhance energy uptake through plasticity induced by phase transformation.[36] Following HIP treatment, the fatigue strength at 8×10^6 cycles has been reported to attain 355 MPa, which is on par with that of conventional heat-treated materials.[29] Therefore, this study used post-processing involving both heat treatment and HIP to examine the differences in structure and material properties of the Ti-6Al-4V alloy manufactured by LPBF in three configurations: As-built compact structure, diamond structure, and gyroid porous structure.

While most reported studies deal with HIP processing of dense AM Ti-6Al-4V alloys, the present study focused on testing HIPed porous structures, which hold promise for use in medical implants. To the best of our knowledge, there is limited information on the HIP processing of porous AM-processed Ti-Al-V alloy. Specifically, diamond and gyroid structures were selected for investigation because they are widely utilized in the medical field. These two types of porous structures differ primarily in the size, shape, and arrangement of struts and in the geometry of interconnected pores between them. Mechanical characterization performed in this study included tensile, compressive, flexural, and hardness testing, accompanied by a detailed structural analysis.

2. Materials and methods

2.1. Materials and processing

For this work, Ti-6Al-4V flat bulk tensile samples (70 × 5 × 3 mm; Figure 1) prepared by the LPBF method were used as reference materials (Table 1). The samples were printed vertically in the LPBF chamber and examined in both the as-printed and HIPed states. The conditions for HIP process (950°C, 2 h, 150 MPa, Argon) were selected according to our preliminary experiments and literature,[37] with the temperature chosen to promote transformation of the martensitic phases to the equilibrium (α + β) structure while limiting grain coarsening.

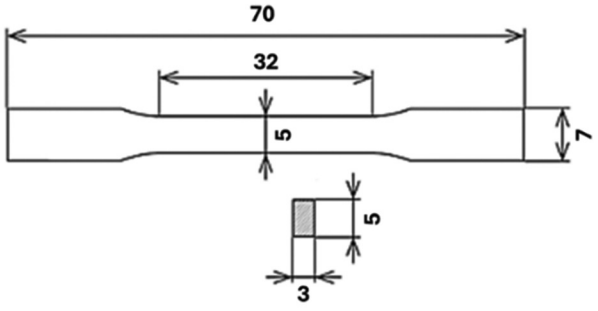

Figure 1. Drawing of printed samples for tensile tests (dimensions given in mm). Reprinted from Strakosova *et al.*[18]

The focus of our research was on the porous structure fabricated by LPBF in two types of structural lattices—diamond and gyroid—which belong to the class of triple periodic minimal surfaces (TPMS). All samples were built on a thin, non-porous substrate. Models of these structures, including elementary cells and larger structures, were generated using the MSLattice program[38] (Figure 2). The computer-aided design (CAD)-generated porosity was set to 70% for both diamond and gyroid types.

The experimental macro-scale porosity was evaluated using the gravimetric method to determine the percentage of free space in the porous structures. The base was removed before weighing, and the sample volume was calculated from measured dimensions. Porosity was determined according to Equation (I):

$$Porosity = 1 - \frac{\rho_{real}}{\rho_{theoretical}} \quad \text{(I)}$$

Where the theoretical density corresponds to the intrinsic material density of Ti-6Al-4V, and the actual density is calculated from the sample's measured mass and geometrical volume.

Using this method, the macroporosity values of 69% (diamond) and 67% (gyroid) were obtained, both of which are in good agreement with the designed value of 70%. Any minor deviations are attributed to imperfections in

Table 1. Supplementary data on the mechanical properties of as-printed and HIPed bulk samples, and porous Ti-6Al-4V samples

Sample	YS (MPa)	UTS (MPa)	E (GPa)	ε (%)	HV1	Micro-porosity (%)
P_AP	1190±8	1283±19	108±7	3±1	353±11	3.62
P_HIP	930±4	1024±3	110±6	17±1	323±7	0.02
Sample	**CYS (MPa)**	**UCS (MPa)**	**CD max (%)**	**UBS (MPa)**	**HV0.5**	**Macro-porosity (%)**
D_AP	81±6	99±1	13±1	164±9	395±18	69
D_HIP	68±2	102±2	16±2	214±35	362±7	66
G_AP	162±5	249±3	23±1	261±10	415±14	67
G_HIP	128±13	222±5	34±1	315±15	316±6	63

Abbreviations: AP: As-printed; CYS: Compressive yield strength; CD max: Maximum compressive deformation; D: Diamond structure; E: Young's modulus; G: Gyroid structure; HIP: Hot isostatic pressing; HV0.5: Vickers hardness (500 g load); HV1: Vickers hardness (1 kg load); UCS: Ultimate compressive strength; UBS: Ultimate bending strength; UTS: Ultimate tensile strength; YS: Yield strength; ε: Elongation.

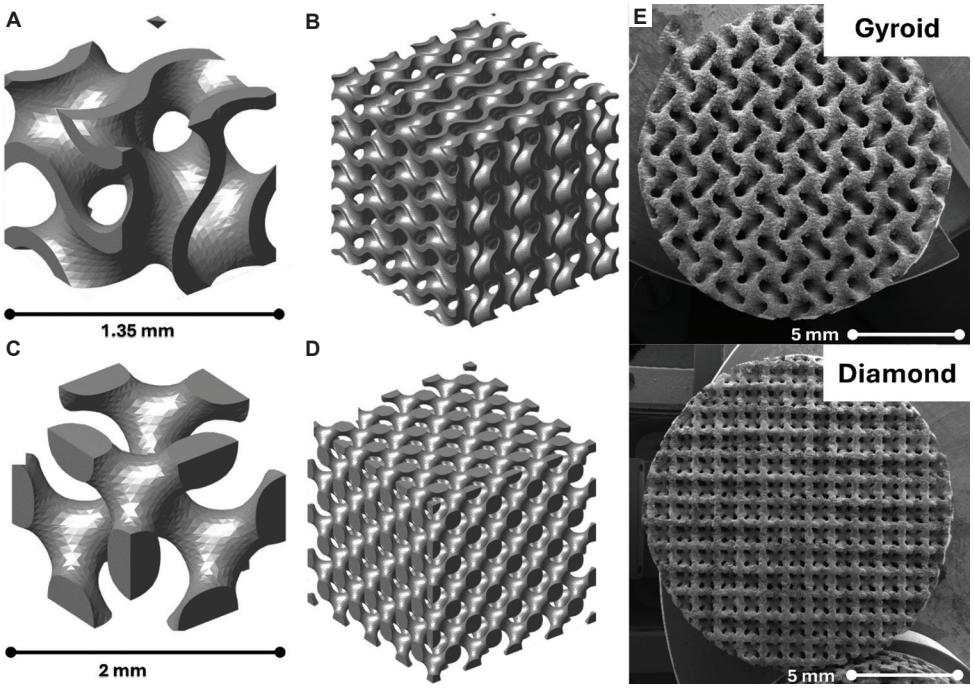

Figure 2. Porous gyroid and diamond structures. (A) Elementary of the cell gyroid structure. (B) Elementary of the diamond cell structure. (C) Gyroid model with multiple elementary cells. (D) Diamond model with multiple elementary cells. (E) Scanning electron microscopy images of diamond and gyroid structures in their as-printed condition. Reprinted from Školáková *et al.*[39]

the LPBF manufacturing process, such as partial melting or powder adhesion.

Both compact and porous samples were printed using a ConceptLaser M2 Cusing printer (ProSpon, Czech Republic) equipped with a 200 W Yb: YAG fiber laser. The printer has a working area of 250 × 250 × 280 mm^3 and operates under a protective argon atmosphere with an oxygen content of up to 0.5% by volume. Continuous mode was used for printing. The scanning speed was 1250 mm/s, the layer thickness was 30 μm, and the hatch spacing was 80 μm.

2.2. Microstructure and porosity

Phase composition of the given samples was determined by X-ray diffraction (XRD) using PANalytical X'Pert PRO system (PANanalytical, Holland) equipped with a copper tube (Kα radiation, λ = 0.15406 nm), Scans were performed over a 2θ range of 5–89° with a step size of 0.039° and a generator setting of 30 mA and 40 kV.

To examine the microstructure, we used a light optical microscope (Nicon, Czech Republic) and scanning electron microscopes (SEM; Tescan Mira, Czech Republic) equipped with energy dispersive spectroscopy (EDS). Metallographic preparation of samples (Figure 3A) included: (i) Sectioning with a cut-off machine (Q-ATM, Germany); (ii) grinding with SiC abrasive sandpapers (P400–P2500, Q-ATM, Germany); (iii) final polishing with a colloidal silica suspension (Eposil F, 0.1 μm; Q-ATM, Germany); LabTest 5.250SP1-VM universal testing machine (LABORTECH s.r.o., Czech Republic) mixed with 4 parts hydrogen peroxide and 1 part water; and (iv) chemical etching with a Croll's solution (2 mL HNO_3 + 98 mL H_2O; Penta, Jersey).

Samples for the measurement of volume porosity were cut from the center of the printed discs, with dimensions of 2.5 × 3 × 15 mm. These dimensions were selected for the resolution and the ability to detect small pores within the matrix. The volume porosity of the samples was determined using micro-computed tomography (μCT; Zeiss Xradia 610 Versa, Carl Zeiss Microscopy, Germany) at a resolution of 4.5 μm/pixel, and the results were analyzed using Dragonfly software (version 2022.1.0.1249).[36] Matrix material, pores within the matrix (matrix pores), and pores intentionally created by TPMS geometry (structural pores) were identified using histogram segmentation (based on pixel intensity) and classified according to pore size. The volume fractions (vol %) of each phase were determined, and mean Feret diameters were calculated for matrix pores.

2.3. Mechanical properties

Mechanical characterization included Vickers hardness (HV1, HV0.5), tensile, compression, and bending tests.

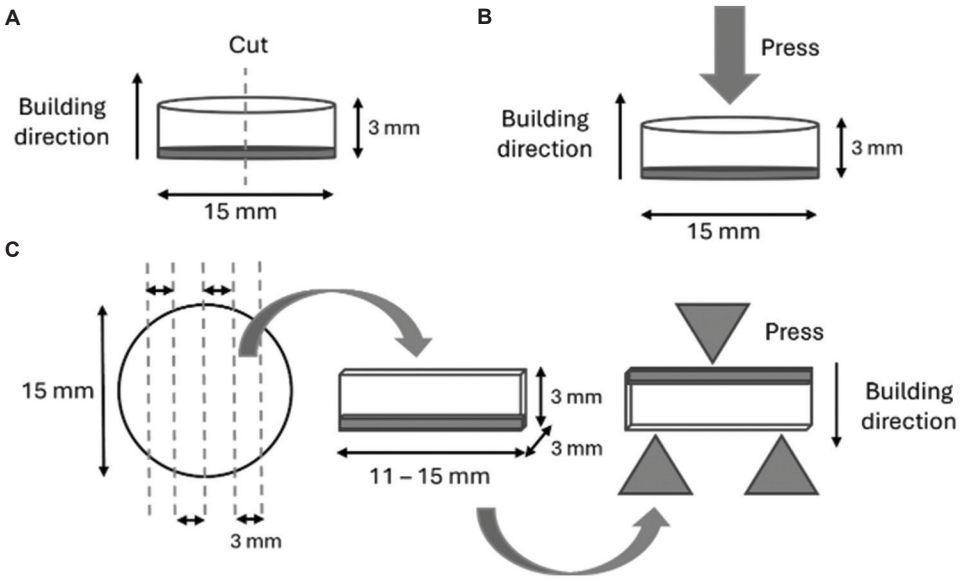

Figure 3. Schematic representations of the test setups. (A) Cutting a sample to create a metallographic cross-section. (B) Uniaxial compression test setup. (C) Specimen preparation for three-point bending tests

These tests were used to evaluate the influence of processing conditions and resulting structure on mechanical performance. For hardness measurements, a minimum of twenty indentations were made on the cross-sections of bulk samples (aligned with the build direction) at various points on a polished surface (P2500 finish). Measurements were taken both on the surface and in cross-section.

An Instron 5882 universal testing machine (Instron Corporation, Germany) with a ±100 kN load cell was used to perform three tensile tests at room temperature for each bulk material. Deformation testing was performed using an MFL 800B extensometer (MF Mess- und Feinwerktechnik GmbH, Velbert, Germany). The specimens were loaded incrementally at a rate of 5 mm/min until failure, after which fracture surfaces were examined using SEM.

Compression and bending tests were carried out on porous diamond and gyroid structures using a LabTest 5.250SP1-VM universal testing machine (Eposil F, 0.1 µm; Q-ATM, Germany); LabTest 5.250SP1-VM universal testing machine (LABORTECH s.r.o., Czech Republic) at room temperature. For each geometry, three compression tests (Figure 3B) and three bending tests (Figure 3C) were performed. Compression properties were evaluated at a constant loading rate of 5 mm/min. Bending tests were conducted using a three-point setup, where two support pins were inserted through the porous section and a third loading pin applied force vertically through the base of the sample (Figure 3C).

The bending test specimens were cut from printed discs into beams with approximate dimensions of 11–15 mm (length) × 3 mm (width) × 3 mm (height). Due to the limited number and small size of samples, a specific ASTM C1161 standard could not be followed for flexural testing. The dense base remained attached and was placed on the compression side (top) during testing. In all cases, the fracture occurred in the porous structure rather than at the base, indicating that the porous region governed the mechanical behavior. The presence of the base may have influenced the stress distribution, which is acknowledged as a limitation of the present test setup.

3. Results

3.1. Microstructure

XRD analysis was performed to analyze the phase composition of the samples (Figure 4). In the as-built condition, all samples exhibited the same phase composition, consisting exclusively of the α′-Ti phase—hexagonal martensite formed during rapid cooling from β-Ti. Following HIP, the α′ phase decomposed into α-Ti and β-Ti phases in both bulk samples and the diamond and gyroid structures. The α-Ti phase corresponds to the hcp allotropic modification of Ti and is difficult to distinguish from α′-Ti due to the near coincidence of their diffraction peaks.

The alloy's initial martensitic microstructure after LPBF is shown in Figure 5A. The fine martensite is characterized by a typical needle-like structure and is accompanied by a high porosity. For the bulk reference material in the as-printed state, the porosity, determined by the gravimetric method, was 3.62 vol % (Table 1), which is

in agreement with literature-reported values for standard LPBF parameters. This porosity likely contributed to the reduced ductility observed in mechanical testing.

After the application of the HIP process, the microstructure underwent significant changes. The martensite phase transformed into a dual-phase α + β titanium structure (Figure 5B).

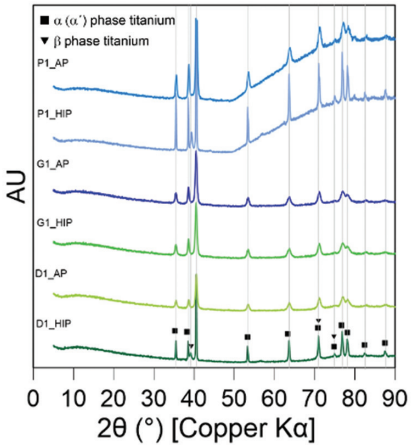

Figure 4. X-ray diffraction (XRD) analysis of the porous samples shows their phase composition
Abbreviations: D_AP: Diamond as-printed sample; D_HIP: Diamond hot isostatically pressed sample; G_AP: Gyroid as-printed sample; G_HIP: Gyroid hot isostatically pressed sample; P_AP: Porous as-printed sample; P_HIP: Porous hot isostatically pressed

Figure 6 shows microstructures of the porous diamond and gyroid structures in the as-printed and HIPed states. In both cross-sections, numerous small internal matrix pores (visible as dark spots) are present within individual struts. HIP transformed the martensite phase into α + β titanium structure and significantly reduced internal porosity to <0.01 vol %.

Figure 7 summarizes the quantitative μCT analysis of pores within the metallic matrix. The analysis focused exclusively on pores fully enclosed by the metallic matrix, excluding the designed macroporosity of the TPMS structures. As shown in Figure 7A, the median Feret diameter of matrix pores decreased after HIP by 38% (from 30.7 μm to 19.0 μm) in the gyroid structure and by 46% (from 30.6 μm to 16.3 μm) in the diamond structure. The total pore count was also markedly reduced—from ~4,400 to ~400. These conclusions are consistent with the volume ratios of pores shown in Figure 7B, illustrating the quantitative description of pores and their mutual relations with the matrix. This comparison is especially important due to potential errors caused by cropping slightly different areas during analysis. For the TPMS structures, the designed macroporosity constituted the largest proportion of sample volume, with minimal impact of the HIP process on this value. In contrast, the matrix pores identified by μCT accounted for up to 1 vol % of the sample volume. These unintended pores were significantly reduced after

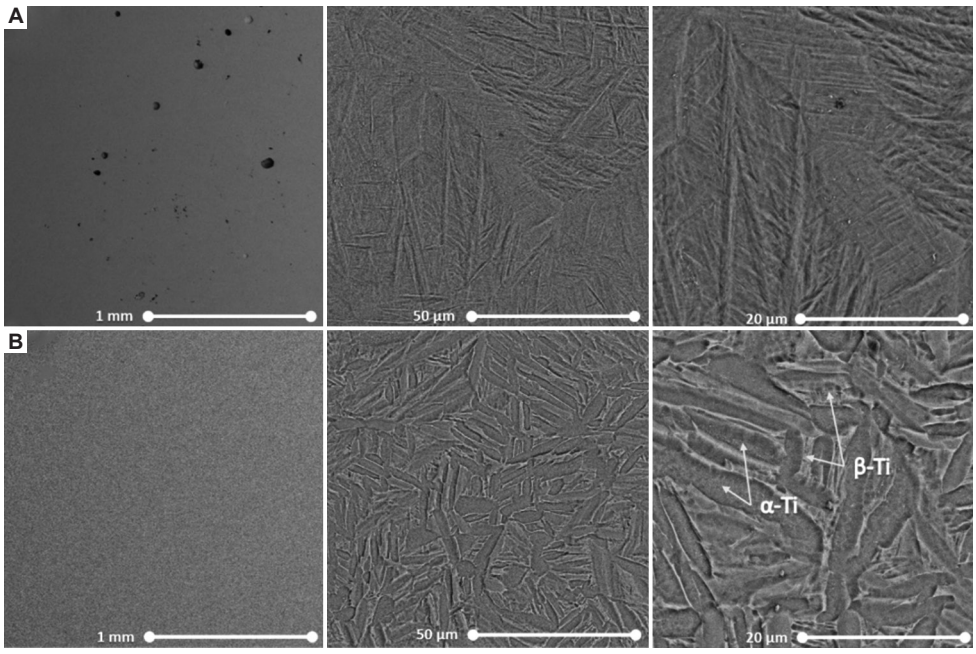

Figure 5. Ti-6Al-4V LPBF microstructure (SEM backscatter). (A) LPBF samples with a needle-like martensitic structure in their as-printed condition. (B) LPBF samples after the HIP process at 950°C and 200 MPa
Abbreviations: α-Ti: α phase titanium; β: β phase titanium; HIP: Hot isostatic pressing; LPBF: laser powder bed fusion; SEM: Scanning electron microscopy

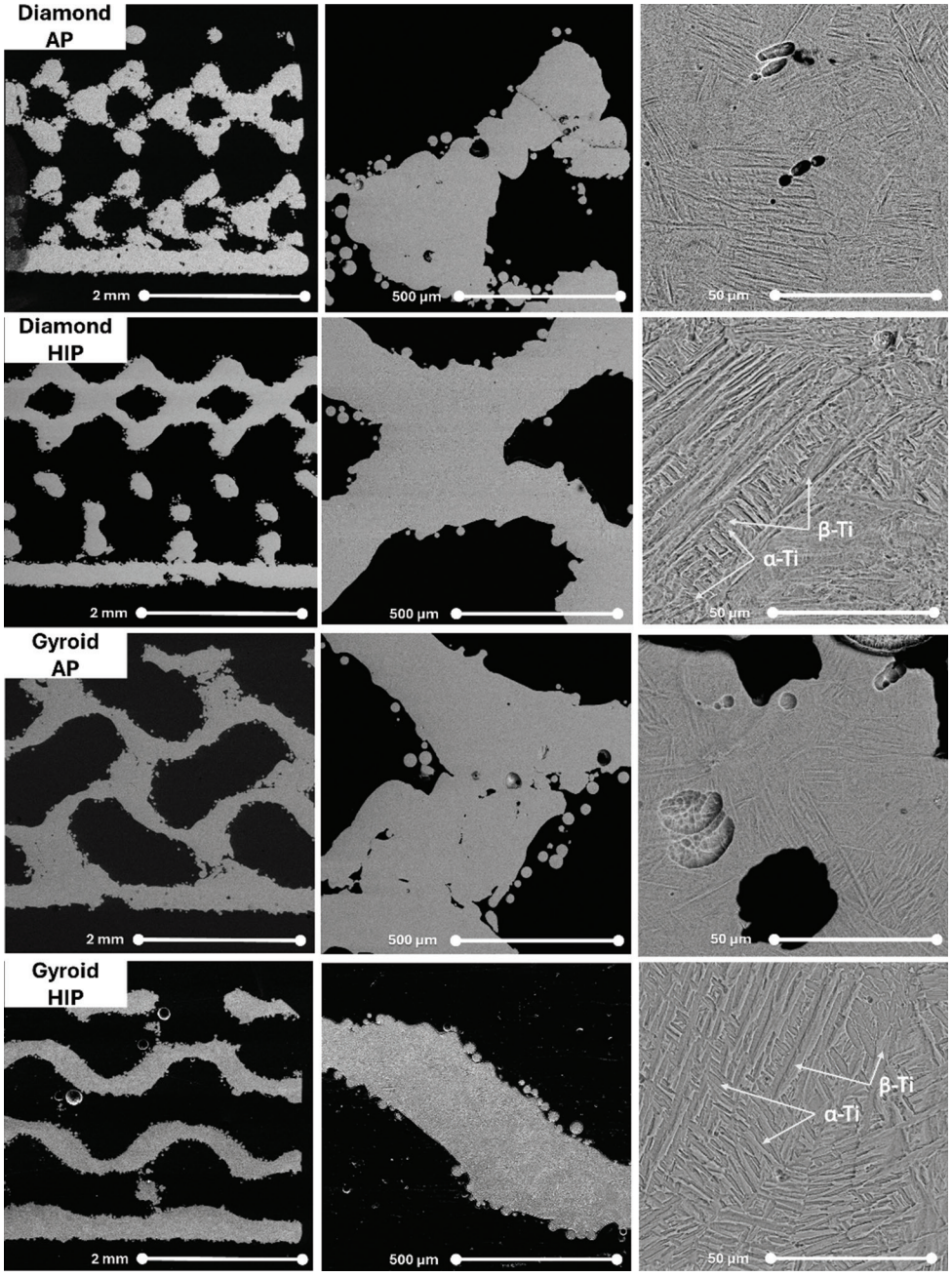

Figure 6. Ti-6Al-4V LPBF porous diamond and gyroid microstructure (SEM back-scattered). Needle-like martensitic structures in the as-printed condition and the corresponding microstructure after HIP at 950°C and 200 MPa

Abbreviations: HIP: Hot isostatic pressing; LPBF: Laser powder bed fusion; SEM: Scanning electron microscopy; α-Ti: α phase titanium; β: β phase titanium

HIP, indicating a strong link to improved mechanical properties. However, μCT was not used to evaluate overall macroporosity in bulk samples.

3.2. Mechanical properties

It is well established that HIP significantly influences the microstructural evolution of Ti-6Al-4V components, particularly by eliminating internal porosity and transforming the martensitic phase into an α + β equilibrium structure. Since the same HIP process was applied to the additively manufactured porous gyroid and diamond scaffolds, it is methodologically sound to first evaluate its effect on the bulk material. Although tensile testing cannot be directly applied to porous samples due

to their complex geometry and limitations in gripping the sample without causing structural damage, testing the bulk material provides an essential reference. The underlying microstructural mechanisms—porosity closure and phase transformation—are shared between the bulk material and the struts of the porous structures. Therefore, testing the mechanical properties of the bulk material is a relevant indicator of the changes in the mechanical response of the scaffold struts post-HIP.

A range of tests was carried out on reference bulk specimens at room temperature to characterize these changes, with the results expressed in terms of hardness measurements (HV1) and uniaxial tensile properties (Figure 8A and Table 1). The HIP-treated samples exhibited a reduction in hardness from 353 HV1 to 323 HV1, reflecting a phase transformation from a fine martensitic microstructure to a more stable α + β configuration. This transformation was also evident in the tensile properties: The as-built condition exhibited high strength (Ultimate tensile strength [UTS] ≈ 1300 MPa) but limited ductility (elongation ≈ 3%), whereas the HIPed samples displayed reduced strength (UTS ≈ 1024 MPa) and substantially improved ductility (elongation ≈ 17%). The results obtained are in line with the microstructural observations and the hardness trend.

Fractographic analysis of the tensile specimens corroborates this interpretation. The fracture surface of the as-built sample exhibited ductile dimples alongside visible, process-induced porosity. In contrast, the HIPed specimen showed uniform ductile fracture morphology with no observable porosity, indicating successful densification of the material (Figure 9).

The mechanical performance of porous gyroid and diamond structures under compressive and flexural loading is summarized in Figure 8B and C, Table 1. The gyroid structure demonstrated superior mechanical behavior compared to the diamond structure, due to its continuous curvature and more uniform stress distribution. HIP treatment enhanced both the compressive strength

A

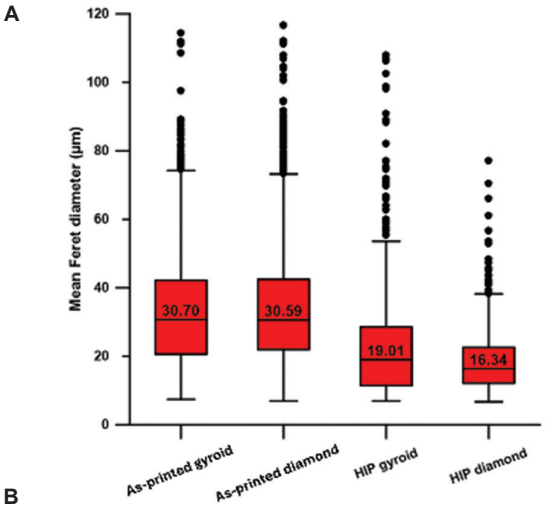

B

Type of ratio	As-printed gyroid	As-printed diamond	HIP gyroid	HIP diamond
	(vol. %)			
Matrix : Matrix pores	0.5	1.0	0.02	0.02
Triply periodic structure pores : Matrix	48.4	42.9	51.2	41.5
Matrix : Triply periodic structures pores	208.6	233.0	186.2	241.0
Triply periodic structure pores : Matrix pores	0.2	0.4	0.01	0.01

Figure 7. Effect of hot isostatic pressing (HIP) on pore size distribution and phase composition in 3D-printed TPMS structures, highlighting changes in Feret diameter and relative fractions of matrix and pores. (A) Box-whisker plot showing the mean Feret diameter of as-printed and HIPed samples. (B) Relative proportions of the matrix, matrix pores, and the intentionally created pores within the printed TPMS structures
Abbreviations: HIP: Hot isostatic pressing; TPMS: Triply periodic minimal surface

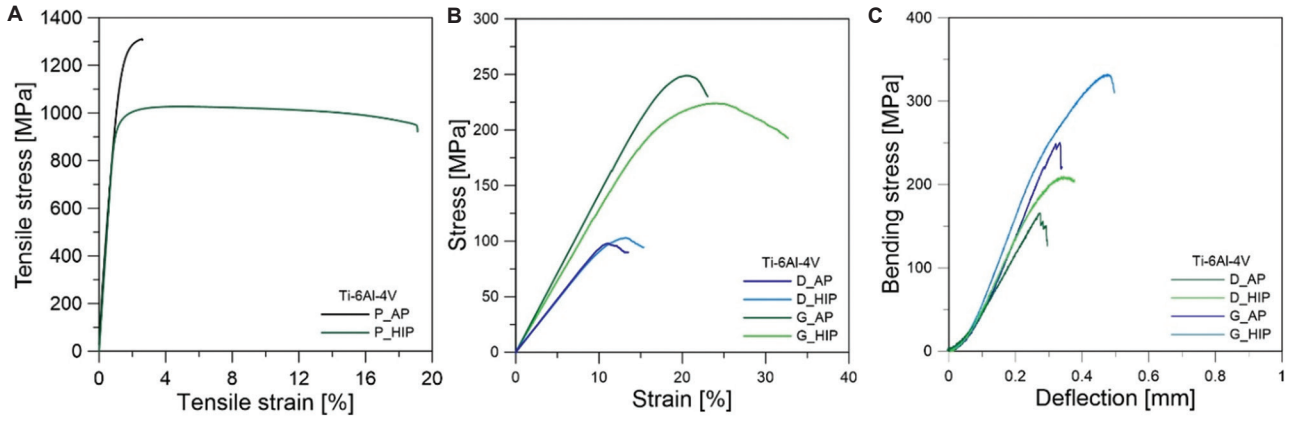

Figure 8. Mechanical properties of the Ti-6Al-4V alloy. (A) Typical stress-strain curves of bulk LPBF samples. (B) Compressive stress-strain curves of the porous samples. (C) Bending stress-strain curves of the porous samples
Abbreviations: D_AP: Diamond as-printed sample; D_HIP: Diamond hot isostatically pressed sample; G_AP: Gyroid as-printed sample; G_HIP: Gyroid hot isostatically pressed sample; LPBF: Laser powder bed fusion; P_AP: Porous as-printed sample; P_HIP: Porous hot isostatically pressed

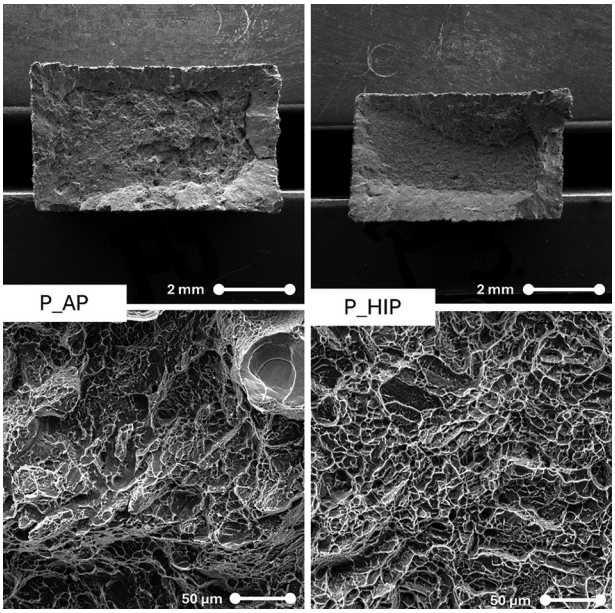

Figure 9. Fracture surfaces of LPBF-produced porous samples before and after HIP treatment. Corresponding high-magnification details of the fracture surfaces are shown below each main image, demonstrating the typical differences in fracture morphology, pore distribution, and surface roughness caused by the HIP
Abbreviations: HIP: Hot isostatically pressed; LPBF: Laser powder bed fusion; P_AP: Porous as-printed sample; P_HIP: Porous hot isostatically pressed

and the plastic deformation capacity of both topologies. For example, the compressive strain of failure increased from 23% to 34% in the gyroid structure. Although there was a slight reduction in ultimate compressive strength (from 249 MPa to 222 MPa), which is likely due to reduced dislocation density and stress relaxation, the increase in ductility is important for applications requiring mechanical reliability under cyclic or impact loading. This is particularly important for biomedical implants, where structural integrity and damage tolerance are essential.

Differences in elastic modulus were also observed between the two types of scaffolds. The gyroid structure exhibited an elastic modulus approximately 1.6 times higher than the diamond structure in the as-built condition and 1.4 times higher after HIP treatment. This reflects the influence of geometric design on stiffness and mechanical anisotropy.

Three-point bending tests (Figure 8C) confirmed the superior flexural performance of gyroid architecture. HIP processing resulted in a ~30% increase in maximum bending stress for both geometries. However, due to progressive micro-fracturing during loading, the stress-strain curves did not display a distinct linear region, which makes precise modulus determination impractical.

SEM of fractured porous samples (Figure 10) revealed residual porosity and unmelted particles in the LPBF condition, primarily in the cores of the struts. After HIP, these defects were eliminated, and the fracture surfaces exhibited fully ductile morphologies dominated by equiaxed dimples. Although macroscopic plastic deformation was not visible during the bending test, the higher fracture strain observed in the HIPed samples compared to the as-built ones is consistent with the tensile test data.

4. Discussion

4.1. Microstructure

The thermal history of Ti-6Al-4V has a significant impact on its microstructure, which in turn is influenced by the applied temperature and cooling rates.[4,40] The LPBF process involves subjecting powdered material to extreme cooling rates (10^3–10^6 K/s). This is achieved by rapidly melting the material with a highly energetic laser beam. This induces a fine acicular martensitic α′ microstructure (Figures 5 and 6) and results in the material having a relatively high residual stress. Directional solidification and repeated thermal cycling during layer formation also lead to pronounced anisotropy.[37-39]

To address these limitations, post-processing methods, such as HIP are commonly employed. HIP simultaneously applies high pressure (>100 MPa) and an elevated temperature (≈920°C for Ti-6Al-4V), which promotes phase transformation (α' → α + β), heals internal defects, and homogenizes the microstructure.[28-30] As demonstrated in previous studies, this process improves ductility and fatigue resistance while reducing anisotropy.[31,41] Although grain coarsening during HIP can cause a slight decrease in tensile and yield strength, the process generally produces a more balanced set of mechanical properties compared to as-built LPBF parts.[42]

However, in the context of porous structures, HIP introduces an additional dimension of complexity: Dimensional stability and structural integrity. Under multiaxial compressive stress and at an elevated temperature, internal pores collapse and surface-connected defects gradually close, leading to a redistribution of material volume. This localized densification can induce slight but significant dimensional changes, particularly in complex porous architectures, such as lattice structures. These changes can affect the geometric fidelity and mechanical response of the final part.

Since pore volume and connectivity vary according to unit cell topology (e.g., gyroid vs. diamond), the magnitude of structural shrinkage may also differ. For

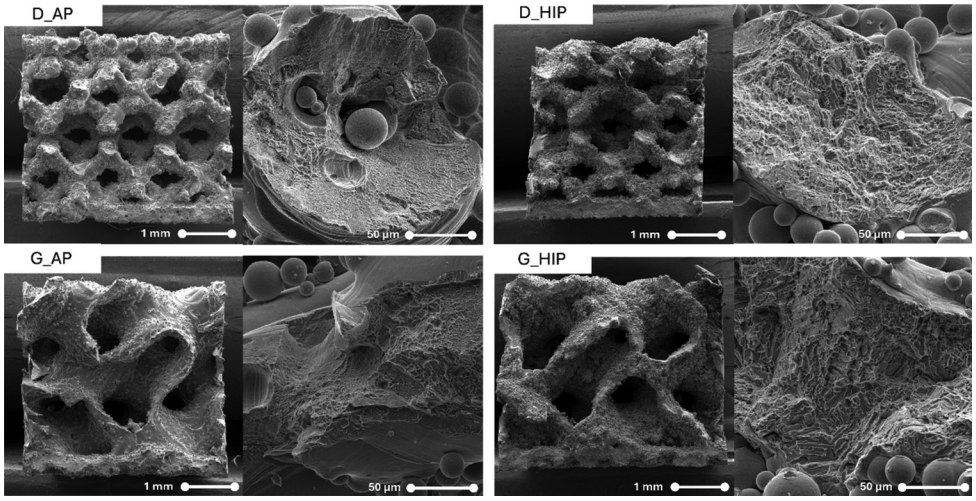

Figure 10. Fracture surfaces of LPBF-fabricated porous structures with diamond and gyroid geometries in the as-printed and HIP-treated states. Corresponding high-magnification details of the fracture surfaces are shown on the right side of each main image
Abbreviations: D_AP: Diamond as-printed sample; D_HIP: Diamond hot isostatically pressed sample; G_AP: Gyroid as-printed sample; G_HIP: Gyroid hot isostatically pressed sample; HIP: Hot isostatically pressed; LPBF: Laser powder bed fusion

example, if the initial pore volume fraction in a diamond scaffold is known from image-based quantification, the change in cross-sectional area or total volume after HIP can be theoretically estimated by subtracting the eliminated porosity from the original scaffold geometry. In practice, however, such changes may lead to a reduction in strut cross-section, alterations in relative density, and deviations from nominal CAD dimensions. Furthermore, the phase transformation from martensite to $\alpha + \beta$ can be accompanied by volumetric contraction. Though this is generally minor in bulk alloys, it can become significant in thin, highly curved features of porous architecture.

Thus, a comprehensive understanding of HIP-induced dimensional evolution is critical for applications requiring high-dimensional precision (e.g., patient-specific implants or load-bearing structures). Future studies may benefit from integrating *in situ* or *ex situ* digital volume correlation or high-resolution μCT to precisely quantify these changes, enabling predictive compensation during the design stage.

4.2. Mechanical properties

As shown in Table 1 and Figure 8, the application of HIP reduces the yield strength, UTS, strain to fracture, and Vickers hardness (HV1) compared with the as-built condition. This reduction is primarily associated with the transformation of the fine martensitic α' structure into a coarser two-phase $\alpha + \beta$ structure during high-temperature exposure in the dissolution annealing region.[35,41] HIP also eliminates internal defects (Figures 5 and 6), but the residual porosity of the material remains a factor influencing the final mechanical response. Porosity affects tensile and bending test performance much more than microhardness and compressive measurements. Therefore, hardness measurements in this study mainly reflect microstructure changes rather than porosity effects.[22] For example, HV1 values in the as-printed state were 395 ± 18 HV0.5 (diamond) and 415 ± 18 HV0.5 (gyroid), compared with 353 ± 11 HV1 for the HIP-treated bulk LPBF specimen (P1_AP) and about 331 ± 7 HV1 for commercial Ti-6Al-4V.[22] The P1_as-built sample is noticeably harder due to the finer lamellar microstructure produced by LPBF rapid cooling. While higher porosity typically reduces strength, pore arrangement and distribution can locally influence hardness. For instance, a fractal-like pore distribution may alter crack initiation and propagation, occasionally increasing local hardness.[42] Processing-induced phase transformations—such as crystallization of initially amorphous powders—can also enhance hardness.[43]

For biomedical Ti-6Al-4V alloy, achieving a UTS between 860 MPa and 1330 MPa and elongation between 10% and 25% is considered acceptable.[44-46] These properties are influenced by microstructure, alloying elements, and precise heat treatment processes, which together ensure the alloy's suitability for medical use. The LPBF as-built specimens in this study achieved UTS of ~1283 MPa, exceeding the lower bound, but with reduced ductility (~6%). After HIP, the UTS decreased to ~1024 MPa, while elongation improved to ~17%, comparable to the as-annealed condition after conventional heat treatment.[4] This strength–ductility trade-off is consistent with other reports showing that laser-based AM parts exhibit strengths comparable to age-hardened Ti-6Al-4V due to

their fine microstructure,[3,47] while HIP shifts properties toward a more ductile profile through microstructural coarsening.

Testing of porous structures was not possible due to their dimensions; therefore, compressive testing was carried out. The reported compressive strength of Ti-6Al-4V implants varies between 186 MPa and 462 MPa, depending on the design and porosity.[48] As shown in Figure 8 and Table 1, the diamond structure exhibited a linear elastic response up to approximately 80 MPa, which corresponds to its compressive yield strength. By contrast, the gyroid structure maintained a linear response up to around 160 MPa, which is also consistent with its measured yield strength. Beyond these points, both structures entered a non-linear deformation associated with plastic collapse. These results align with previous findings, such as Barui *et al.*,[49] who reported approximately 200 MPa compressive strength for microporous cylinders (Young's modulus ~4 GPa), and Li *et al.*,[50] who showed a compressive strength of 194.6 MPa for a porous Ti-6Al-4V implant—comparable to the gyroid structure here. The present porous specimens exhibited strengths of 47.0 ± 12.1 MPa (diamond) and 90.0 ± 4.0 MPa (gyroid).

The designed porosity for both diamond and gyroid structures was 64–72%, depending on lattice geometry (Figures 5 and 6). Such controlled porosity reduces stress shielding and promotes osseointegration, with the target of approximating natural bone stiffness for long-term implant stability.[53,54] HIP treatment reduced microporosity—potential crack initiation sites—thereby improving material integrity. However, this densification also slightly reduced UCS by modifying load distribution within the lattice. As expected, the compressive performance of porous lattices remains substantially below that of dense Ti-6Al-4V,[23] even though hardness values between porous and bulk specimens were comparable.

The study also included three-point bending tests to assess the stiffness and flexural strength of the porous implant. The results showed the same trend as the compressive tests, with the porous diamond structure exhibiting lower performance compared to the gyroid structure (Figure 8), which achieved a higher UBS (Table 1). For both structures, the HIP treatment led to an improvement in the UBS value (diamond: 164–214 MPa; gyroid: 261–315 MPa). The results of Suresh *et al.*[51] similarly showed that LPBF-produced porous Ti-6Al-4V implants have low stiffness and high porosity, favorable for biomedical applications, with reduced stiffness (80 GPa) and increased cell proliferation. Compared to Li *et al.*[50] (max bending strength 126.3 MPa), both porous structures in this study achieved higher bending strength in both the as-built and HIP conditions.

Interestingly, the improvement in mechanical performance following HIP is not uniform across all loading modes and scaffold geometries. For instance, gyroid structures demonstrated a substantial increase in flexural strength, whereas diamond structures exhibited only modest enhancement. This divergence may be attributed to differences in stress distribution under bending, influenced by unit cell design and load-bearing pathways. Furthermore, localized densification effects induced by HIP may benefit certain geometries more than others, depending on their internal curvature and pore connectivity.

Previous work highlights further distinctions in failure modes: Diamond lattices tend to fail abruptly through sudden strut buckling, whereas gyroid lattices fail more gradually through progressive wall collapse.[52] Thus, scaffold geometry strongly influences mechanical behavior and overall performance. Although a full mechanistic analysis was beyond the scope of this work, these observations underscore the importance of tailoring post-processing strategies, such as HIP, to both geometry and loading conditions.

5. Conclusion

This study examined the effect of HIP post-processing on the microstructure and mechanical properties of Ti-6Al-4V manufactured by LPBF. The key findings are: (1) HIP at 950°C transformed martensite α' into a two-phase α + β structure; (2) Pores produced during LPBF were reduced in volume; (3) Microstructural changes reduced mechanical properties but increased ductility; and (4) The applied post-processing treatment effectively reduced microporosity not only in bulk samples but also in porous scaffold structures, leading to improved mechanical properties. While further optimization of AM parameters may enhance the quality of porous structures, the present results demonstrate HIP's significant positive impact on both types of samples.

Acknowledgments

We gratefully acknowledge Jan Drahokoupil for his assistance with the micro-CT measurements.

Funding

This work was supported by the project "Mechanical Engineering of Biological and Bioinspired Systems" (Project No. CZ.02.01.01/00/22_008/0004634) funded

by "Programme Johannes Amos Commenius," Excellent Research Call. It was also supported by the Ministry of Health of the Czech Republic in cooperation with the Czech Health Research Council (Project No. NW25-08-00044). The authors also acknowledge the grant of Specific University Research (Grant No. A1_FCHT_2025_011).

Conflicts of interest

The authors declare that they have no competing interests.

Author contributions

Conceptualization: Dalibor Vojtech and Marketa Strakova
Investigation: Marketa Strakova, Jonas Divin, and Jan Drahokoupil
Methodology: Marketa Strakova, Jiri Kubasek, and Jan Pinc
Writing – original draft: Marketa Strakova
Writing – review and editing: Jiri Kubasek, Jan Pinc, and Dalibor Vojtech

Ethics approval and consent to participate

Not applicable.

Consent for publication

Not applicable.

Availability of data

The data are accessible through the Zenodo repository: https://doi.org/10.5281/zenodo.16794521

References

1. Pushp P, Dasharath SM, Arati C. Classification and applications of titanium and its alloys. *Mater Today Proc*. 2022;54(2):537-542.

   doi: 10.1016/j.matpr.2022.01.008

2. Elitzer D, Jäger S, Höll C, *et al*. Development of microstructure and mechanical properties of TiAl6V4 processed by wire and arc additive manufacturing. *Adv Eng Mater*. 2022;25:2201025.

   doi: 10.1002/adem.202201025

3. Carroll BE, Palmer TA, Beese AM. Anisotropic tensile behavior of Ti-6Al-4V components fabricated with directed energy deposition additive manufacturing. *Acta Mater*. 2015;87:309-320.

   doi: 10.1016/j.actamat.2014.12.054

4. Donachie MJ. *Titanium: A Technical Guide*. United States: ASM International; 2000. p. 369.

5. Etesami SA, Fotovvati B, Asadi E. Heat treatment of Ti-6Al-4V alloy manufactured by laser-based powder-bed fusion: Process, microstructures, and mechanical properties correlations. *J Alloys Compds*. 2022;895:162618.

   doi: 10.1016/j.jallcom.2021.162618

6. Mohammed MT. Mechanical properties of SLM-titanium materials for biomedical applications: A review. *Mater Today Proc*. 2018;5(Pt 3):17906-17913.

   doi: 10.1016/j.matpr.2018.06.119

7. Gu DD, Shen Y, Popovich VA, Wissenbach K. Laser additive manufacturing of metallic components: Materials, processes and mechanisms. *Int Mater Rev*. 2012;57(3):133-164.

   doi: 10.1179/1743280411Y.0000000014

8. Mueller B. Additive manufacturing technologies-rapid prototyping to direct digital manufacturing. *Assembly Automat*. 2012;32(2).

   doi: 10.1108/aa.2012.03332baa.010

9. Frazier WE. Metal additive manufacturing: A review. *J Mater Eng Perform*. 2014;23(6):1917-1928.

   doi: 10.1007/s11665-014-0958-z

10. Dutta B, Froes FH. Additive manufacturing of titanium alloys. *AMP Tech Artic*. 2014;172(2):18-23.

11. Hollander DA, Perez MC, Brinkmann M, *et al*. Structural, mechanical and *in vitro* characterization of individually structured Ti-6Al-4V produced by direct laser forming. *Biomaterials*. 2006;27(7):955-963.

    doi: 10.1016/j.biomaterials.2005.07.041

12. Leuders S, Thone M, Riemer A, *et al*. On the mechanical behavior of titanium alloy TiAl6V4 manufactured by selective laser melting: Fatigue resistance and crack growth performance. *Int J Fatigue*. 2013;48:300-307.

    doi: 10.1016/j.ijfatigue.2012.11.011

13. Das S, Zhang GD, Li H, *et al*. Processing of titanium net shapes by SLS/HIP. *Mater Design*. 1999;20(2):115-121.

14. Vilaro T, Colin C, Bartout JD. As-fabricated and heat-treated microstructures of the Ti-6Al-4V alloy processed by selective laser melting. *Metall Mater Trans A*. 2011;42(10):3190-3199.

    doi: 10.1007/s11661-011-0731-y

15. Bai L, Chen Y, Cheng N, *et al*. Effects of heat treatment and hot isostatic pressing on microstructure and fatigue improvements in Ti-6Al-4V alloy fabricated by selective laser melting. *Mater Lett*. 2024;367:136641.

    doi: 10.1016/j.matlet.2024.136641

16. Yadav BN, Lin DW, Lin MC, *et al*. Implemented *in-situ* heat treatment process for controlling the residual thermal stresses during the fabrication of Ti-6Al-4V titanium alloy through additive manufacturing. *Mater Lett*. 2024;356:135580.

    doi: 10.1016/j.matlet.2023.135580

17. Huang G, Gu D, Liu H, Lin K, Wang R, Sun H. The role of graded layers in interfacial characteristics and mechanical properties of Ti6Al4V/AlMgScZr-graded multi-material parts fabricated using laser powder bed fusion. *Mater Sci*

Addit Manuf. 2024;3(2):3088.

doi: 10.36922/msam.3088

18. Strakosova A, Kubásek J, Michalcová A, Průša F, Vojtěch D, Dvorský D. High strength X3NiCoMoTi 18-9-5 maraging steel prepared by selective laser melting from atomized powder. *Materials* (*Basel*). 2019;12:4174.

    doi: 10.3390/ma12244174

19. Herzog D, Seyda V, Wycisk E, Emmelmann C. Additive manufacturing of metals. *Acta Mater*. 2016;117:371-392.

    doi: 10.1016/j.actamat.2016.07.019

20. Shi J, Liang H, Jiang J, Tang W, Yang J. Design and performance evaluation of porous titanium alloy structures for bone implantation. *Math Problems Eng*. 2019;2019:5268280.

    doi: 10.1155/2019/5268280

21. Yue X, Tang H, Lu S, *et al*. Impact behavior of AlSi10Mg porous structures with varying single-unit cell rotation angles fabricated via laser powder bed fusion. *MSAM*. 2025;4(2):025130019.

    doi: 10.36922/MSAM025130019

22. Fousová M, Vojtěch D, Kubásek J, Jablonská E, Fojt F. Promising characteristics of gradient porosity Ti-6Al-4V alloy prepared by SLM process. *J Mech Behav Biomed Mater*. 2017;69:368-376.

    doi: 10.1016/j.jmbbm.2017.01.043

23. Wang B, Luo M, Shi Z, *et al*. Porous titanium alloys for medical application: Progress in preparation process and surface modification research. *MSAM*. 2024;3(1):2753.

    doi: 10.36922/msam.2753

24. Gao X, Zhao Y, Wang M, Liu Z, Liu C. Parametric design of hip implant with gradient porous structure. *Front Bioeng Biotechnol*. 2022;10:850184.

    doi: 10.3389/fbioe.2022.850184

25. Verma R, Kumar J, Singh N, *et al*. Low elastic modulus and highly porous triply periodic minimal surfaces architectured implant for orthopedic applications. *Proc Instit Mech Eng E J Process Mech Eng*. 2022;239(4):1553-1561.

    doi: 10.1177/09544089221111258

26. Roudnicka M, Mertova K, Vojtech D. Influence of hot isostatic pressing on mechanical response of as-built SLM titanium alloy. *IOP Conf Ser Mater Sci Eng*. 2019;629(1):012034.

    doi: 10.1088/1757-899X/629/1/012034

27. Alcisto J, Enriquez A, Garcia H, *et al*. Tensile properties and microstructures of laser-formed Ti-6Al-4V. *J Mater Eng Perform*. 2011;20:203-212.

    doi: 10.1007/s11665-010-9670-9

28. Amsterdam E, Kool G. High cycle fatigue of laser beam deposited Ti-6Al-4V and Inconel 718. In: *Proceedings of the 25th Symposium of the International Committee on Aeronautical Fatigue (ICAF)*. Rotterdam, The Netherlands: Springer; 2009.

29. Alegre JM, Díaz A, García R, Peral LB, Cuesta II. Effect of HIP post-processing at 850 °C/200 MPa in the fatigue behavior of Ti-6Al-4V alloy fabricated by selective laser melting. *Int J Fatigue*. 2022;163:107097.

    doi: 10.1016/j.ijfatigue.2022.107097

30. Ma HY, Wang JC, Qin P, *et al*. Advances in additively manufactured titanium alloys by powder bed fusion and directed energy deposition: Microstructure, defects, and mechanical behavior. *J Mater Sci Technol*. 2024;183:32-62.

    doi: 10.1016/j.jmst.2023.11.003

31. Wang Y, Liu X, Zhang X, *et al*. Cell-size graded sandwich enhances additive manufacturing fidelity and energy absorption. *Int J Mech Sci*. 2021;211:106798.

    doi: 10.1016/j.ijmecsci.2021.106798

32. Wu MW, Lai PH. The positive effect of hot isostatic pressing on improving the anisotropies of bending and impact properties in selective laser melted Ti-6Al-4V alloy. *Mater Sci Eng A*. 2016;658:429-438.

    doi: 10.1016/j.msea.2016.02.023

33. Wu MW, Chen JK, Lin BH, Chiang PH. Improved fatigue endurance ratio of additive manufactured Ti-6Al-4V lattice by hot isostatic pressing. *Mater Design*. 2017;134:163-170.

    doi: 10.1016/j.matdes.2017.08.048

34. Lee J, Ha H, Seol JB, *et al*. Reverse effect of hot isostatic pressing on high-speed selective laser melted Ti-6Al-4V alloy. *Mater Sci Eng A*. 2021;807:140880.

    doi: 10.1016/j.msea.2021.140880

35. Lv Z, Li H, Che L, *et al*. Effects of HIP process parameters on microstructure and mechanical properties of Ti-6Al-4V fabricated by SLM. *Metals*. 2023;13:991.

    doi: 10.3390/met13050991

36. Yan X, Yue S, Ge J, Chen C, Lupoi R, Yin S. Microstructural and mechanical optimization of selective laser melted Ti6Al4V lattices: Effect of hot isostatic pressing. *J Manuf Process*. 2022;77:151-162.

    doi: 10.1016/j.jmapro.2022.02.024

37. Xu Q, Chen B, Bai Q, *et al*. Effects of hot isostatic pressing temperature on casting shrinkage densification and microstructure of Ti6Al4V alloy. *China Foundry*. 2017;14(5):429-434.

    doi: 10.1007/s41230-017-7178-8

38. Alketan O, Abu Al-Rub RK. MSLattice: A free software for generating uniform and graded lattices based on triply periodic minimal surfaces. *Mater Design Process Commun*. 2020;3:e205.

39. Školáková A, Pinc J, Kubik R, *et al*. The effect of pulsed laser on the surface state of 3D-printed triply periodic structures in TiAl6V4 alloy. *Prog Addit Manuf*. 2025.

doi: 10.1007/s40964-025-01254-7

40. Technologies Canada Inc. *DragonflyComet*. Montreal, Canada: Technologies Canada Inc.; 2022.

41. Su C, Yu H, Wang Z, Yang J, Zeng X. Controlling the tensile and fatigue properties of selective laser melted Ti-6Al-4V alloy by post treatment. *J Alloys Compds*. 2021;857:157552.

doi: 10.1016/j.jallcom.2020.157552

42. Kuang DM, Long ZL, Ogwu I, Kuang FL, Yang LM. DEM study on the effect of pore characteristic on single particle crushing behavior of porous particles. *Comput Geotechnics*. 2024;165:105919.

doi: 10.1016/j.compgeo.2023.105919

43. Pilliar RM, Filiaggi MJ, Wells JD, Grynpas MD, Kandel RA. Porous calcium polyphosphate scaffolds for bone substitute applications -- *in vitro* characterization. *Biomaterials*. 2001;22(9):963-972.

doi: 10.1016/s0142-9612(00)00261-1

44. Ji R, Zhang H, Chen L, Cheng L, Luo H, Mao J. Improving the strength and maintaining good ductility of as-forged Ti6Al4V alloy by regulating the microstructural defects. *Mater Sci Eng A*. 2024;911:146913.

doi: 10.1016/j.msea.2024.146913

45. Li J, Liu X, Luo X, *et al*. Overcoming the strength-ductility trade-off and anisotropy of mechanical properties of Ti6Al4V with electron beam powder bed fusion. *Mater Sci Eng A*. 2023;879:145301.

doi: 10.1016/j.msea.2023.145301

46. Liu J, Sun Q, Zhou C, *et al.* Achieving Ti6Al4V alloys with both high strength and ductility via selective laser melting. *Mater Sci Eng A*. 2019;766:138319.

doi: 10.1016/j.msea.2019.138319

47. Vrancken B, Thijs L, Kruth JP, Van Humbeeck J. Heat treatment of Ti6Al4V produced by selective laser melting: Microstructure and mechanical properties. *J Alloys Compds*. 2012;541:177-185.

doi: 10.1016/j.jallcom.2012.07.022

48. Gain AK, Cui Y, Zhang L. Pore-gradient Ti6Al4V alloy mimicking the properties of human cortical bones: The design of TPMS structures by selective laser melting. *Mater Sci Eng A*. 2024;915:147220.

doi: 10.1016/j.msea.2024.147220

49. Barui S, Chatterjee S, Mandal S, Kumar A, Basu B. Microstructure and compression properties of 3D powder printed Ti-6Al-4V scaffolds with designed porosity: Experimental and computational analysis. *Mater Sci Eng C Mater Biol Appl*. 2017;70:812-823.

doi: 10.1016/j.msec.2016.09.040

50. Li X, Wang CT, Zhang WG, Li YC. Properties of a porous Ti-6Al-4V implant with a low stiffness for biomedical application. *Proc Inst Mech Eng H*. 2009;223(2):173-178.

doi: 10.1243/09544119JEIM466

51. Suresh S, Sun CN, Tekumalla S, Rosa V, Ling Nai SM, Wong RC. Mechanical properties and *in vitro* cytocompatibility of dense and porous Ti-6Al-4V ELI manufactured by selective laser melting technology for biomedical applications. *J Mech Behav Biomed Mater*. 2021;123:104712.

doi: 10.1016/j.jmbbm.2021.104712

52. Timercan A, Sheremetyev V, Brailovski V. Mechanical properties and fluid permeability of gyroid and diamond lattice structures for intervertebral devices: Functional requirements and comparative analysis. *Sci Technol Adv Mater*. 2021;22:285-300.

doi: 10.1080/14686996.2021.1907222

53. Anatolie, T.; Sheremetyev, V.; Brailovski, V., Mechanical properties and fluid permeability of gyroid and diamond lattice structures for intervertebral devices: Functional requirements and comparative analysis. Science and Technology of Advanced Materials 2021, 22.

54. Naghavi, S. A.; Tamaddon, M.; Garcia-Souto, P.; Moazen, M.; Taylor, S.; Hua, J.; Liu, C., A novel hybrid design and modelling of a customised graded Ti-6Al-4V porous hip implant to reduce stress-shielding: An experimental and numerical analysis. Front Bioeng Biotechnol 2023, 11, 1092361.